

TITLE

The noncoding circular RNA *circHomer1* regulates developmental experience-dependent plasticity in mouse visual cortex

AUTHORS

Kyle R. Jenks^{1,11}, Ying Cai^{2,11}, Marvin Eduarte Nayan^{3,10}, Katya Tsimring¹, Keji Li¹, José C. Zepeda¹, Gregg R. Heller¹, Chloe Delepine¹, Jennifer Shih¹, Shiyang Yuan², Yao Zhu², Ye Wang⁴, Yangyang Duan⁴, Amy K. Y. Fu⁴, Taeyun Ku⁵, Dae Hee Yun¹, Kwanghun Chung¹, Chi Zhang⁶, Edward S. Boyden^{6,7}, Nikolaos Mellios^{8,9}, Mriganka Sur^{*1}, Jacque Pak Kan Ip^{*2,10}

AFFILIATIONS

¹Department of Brain and Cognitive Sciences, The Picower Institute for Learning and Memory, Massachusetts Institute of Technology, Cambridge, Massachusetts, 02139, USA

²School of Biomedical Sciences, The Chinese University of Hong Kong, Hong Kong, China.

³Department of Biology, Massachusetts Institute of Technology, Cambridge, Massachusetts, 02139, USA

⁴Division of Life Science, The Hong Kong University of Science and Technology, Clear Water Bay, Hong Kong, China.

⁵Graduate School of Medical Science and Engineering, Korea Advanced Institute of Science and Technology, Daejeon, Korea.

⁶Department of Brain and Cognitive Sciences, McGovern Institute for Brain Research, Massachusetts Institute of Technology, Cambridge, Massachusetts, 02139, USA

⁷Howard Hughes Medical Institute, Cambridge, Massachusetts, 02139, USA

⁸Circular Genomics Inc, Albuquerque, New Mexico, 87110, USA

⁹Previously at: University of New Mexico, Department of Neurosciences, Albuquerque, New Mexico, 87131, USA

¹⁰Gerald Choa Neuroscience Institute, The Chinese University of Hong Kong, Hong Kong, China.

¹¹These authors contributed equally

*Address correspondence to Jacque Pak Kan Ip (jacqueip@cuhk.edu.hk) and Mriganka Sur (msur@mit.edu)

Abstract

Circular RNAs (circRNAs) are noncoding RNAs abundant in brain tissue, and many are derived from activity-dependent, linear mRNAs encoding for synaptic proteins, suggesting that circRNAs may directly or indirectly play a role in regulating synaptic development, plasticity, and function. However, it is unclear if the circular forms of these RNAs are similarly regulated by activity and what role these circRNAs play in developmental plasticity. Here, we employed transcriptome-wide analysis comparing differential expression of both mRNAs and circRNAs in juvenile mouse primary visual cortex (V1) following monocular deprivation (MD), a model of developmental plasticity. Among the differentially expressed mRNAs and circRNAs following 3-day MD, the circular and the activity-dependent linear forms of the *Homer1* gene, *circHomer1* and *Homer1a* respectively, were of interest as their expression changed in opposite directions: *circHomer1* expression increased while the expression of *Homer1a* decreased following MD. Knockdown of *circHomer1* prevented the depression of closed-eye responses normally observed after 3-day MD. *circHomer1*-knockdown led to a reduction in average dendritic spine size prior to MD, but critically there was no further reduction after 3-day MD, consistent with impaired structural plasticity. *circHomer1*-knockdown also prevented the reduction of surface AMPA receptors after 3-day MD. Synapse-localized puncta of the AMPA receptor endocytic protein Arc increased in volume after MD but were smaller in *circHomer1*-knockdown neurons, suggesting that *circHomer1* regulates plasticity through mechanisms of activity-dependent AMPA receptor endocytosis. Thus, activity-dependent circRNAs regulate developmental synaptic plasticity, and our findings highlight the essential role of *circHomer1* in V1 plasticity induced by short-term MD.

Keywords

circular RNA; primary visual cortex; critical period; ocular dominance plasticity; synaptic plasticity

Significance Statement

Circular RNAs (circRNAs) are a class of closed-loop RNAs formed through back-splicing of exon and/or intron junctions. Initially considered as byproducts of aberrant RNA splicing with limited function, recent studies have implicated circRNAs in various neurological disorders. Despite their abundant expression in the brain, the role of circRNAs in synaptic function and plasticity remain poorly understood. We conducted an *in vivo* transcriptome analysis of circRNAs whose expression was regulated by experience-dependent plasticity in visual cortex and found that *circHomer1*, a circRNA derived from the *Homer1* gene, is critical for functional plasticity *in vivo*. Developmentally regulated *circHomer1* mediates synaptic plasticity via Arc-mediated endocytosis of AMPA receptors. Our findings demonstrate circRNA regulation during experience-dependent plasticity and reveal their functional significance and mechanism.

Introduction

Neuronal plasticity is a tightly regulated process that requires orchestrated gene transcription to form mRNAs that are subsequently translocated and translated into proteins to induce the functional and structural reorganization of synapses(1). Though we now know a great deal about the mRNAs recruited by and required for synaptic plasticity, it remains unclear if the various forms of non-coding RNAs are as tightly regulated as their protein-coding counterparts, or indeed if these non-coding RNAs are capable of contributing to plasticity(2). Recent RNA-sequencing screens have shown that a plethora of genes that produce alternatively spliced mRNAs also generate non-coding isoforms composed of backspliced and covalently-joined exons and/or introns known as circular RNAs (circRNAs)(3). Although much is still unknown about the precise mechanisms that govern the biogenesis, regulation, and function of circRNAs; there is emerging evidence that circRNAs may have important roles in the brain(2, 4). They are dynamically expressed during brain development, are localized to synapses(5), and a small number of circRNAs have been shown to affect neuronal gene expression, miRNA availability, and regulate behavior(6, 7). However, it remains unclear if circRNAs play a role in regulating synaptic plasticity.

Ocular dominance plasticity in mouse primary visual cortex (V1) is a well-defined model of cortical plasticity induced by monocular deprivation (MD), typically via suture of the eye-lids, during a developmental critical period(8–13). During this window, which in mice begins at postnatal day (P)21 and ends around P35(14), MD induces a reduction of V1 responses to the deprived eye after ~3days of deprivation, followed by an increase of responses to the non-deprived eye(15) after ~7days of deprivation(9, 11–13, 16–18). MD also leads to the activity-dependent up- and down-regulation of many mRNAs known to regulate synaptic plasticity(8–13). Thus, we sought to use MD to identify circRNAs in mouse V1 that could be similarly involved in regulating synaptic plasticity and function.

By screening for differentially expressed mRNA and circRNAs in the developing mouse V1 following 3 days of MD (3-day MD), we discovered that the expression of linear and circular *Homer1* RNA exhibited opposite changes during 3-day MD, suggesting a specific role for the circular *Homer1* variant (*circHomer1*) in MD. Using

circHomer1-specific *in vivo* knockdown in V1, we showed that *circHomer1* is necessary for normal closed-eye response depression and spine shrinkage following 3-day MD. Knockdown of *circHomer1* also impaired downregulation of the AMPA receptor subunit GluA1 following 3-day MD, putatively by reducing Arc protein expression at dendritic spines. In contrast, at 7-day MD knockdown of *circHomer1* had no effect on ocular dominance plasticity, spine size, or AMPA receptor expression compared to controls. Together, these data provide the first evidence of an experience-dependent circRNA that is required for synaptic plasticity induced by short-term MD.

Results

circRNA expression is regulated by experience-dependent plasticity

To identify potential activity-regulated circRNAs, we performed MD in mice beginning at P25, collected tissue from V1 both contralateral and ipsilateral (control) to the deprived eye, and examined the transcriptomic profile after 3-day MD (Fig. 1A). Before exploring the circRNA expression profile, we first conducted mRNA sequencing to validate our protocol against previously observed mRNA regulation by MD. We compared V1 RNA expression between the hemisphere contralateral to the deprived eye, where the majority of change in synaptic drive occurs, normalized to the ipsilateral hemisphere which receives significantly less input from the deprived eye. We identified a total of 1173 differentially-expressed mRNAs, with more mRNAs downregulated than upregulated (472 upregulated and 701 downregulated, Fig. 1B). mRNAs known to be downregulated during MD, such as *Bdnf* and *Nptx2*(20), were also downregulated in our data (Supplementary Table 1). Gene Ontology (GO) analysis showed that the differentially-expressed mRNAs were enriched for synaptic functions (Fig. 1D). Having confirmed that our preparation replicated the known regulation of mRNA expression by 3-day MD(19), we next performed standard short-read RNA-sequencing with the same set of RNA samples. We used a published circRNA alignment tool, *circTools*, to detect circRNA transcripts by virtue of their unique out-of-order junctional reads(20). A total of 1489 unique circRNAs were detected, with 73 differentially-expressed (Fig. 1C, Supplementary Table 2). Of the differentially-expressed circRNAs, we observed 27 significantly upregulated circRNAs and 46 downregulated circRNAs. Some of the

genes from which these differentially-expressed circRNAs were derived have known roles in synaptic plasticity and function (Supplementary Fig. 1A). Indeed, we also identified changes in the corresponding mRNA isoforms of several differentially expressed circRNAs. Of these, the linear isoforms of *circHomer1*, *circPrkce*, and *circDcun1d4* were of interest as they exhibited changes in the opposite direction compared to their circular counterparts (Fig. 1E).

We also performed a transcriptomic analysis of mRNAs and circRNAs in V1 after 7-day MD (Supplementary Fig. 1B-F and Supplementary Tables 3 and 4). *circPrkce*, *circDcun1d4*, and their linear isoforms were not differentially expressed at this timepoint. Intriguingly, after 7-day MD, *circHomer1* and its linear counterpart *Homer1a* were now both found to be downregulated. Based on these findings, and the known role of *Homer1a* in synaptic plasticity, we chose to more closely examine the activity-dependent regulation and role of *circHomer1* in V1 plasticity.

***circHomer1* expression is developmentally regulated**

circHomer1 is composed of exons 2 through 5 of the *Homer1* gene, with backsplicing between exon 2 and 5 (Fig. 2A). Using probes targeting the backsplice junction of *circHomer1*, we employed Expansion FISH (ExFISH)(21) to confirm *circHomer1* localization in V1 neurons (Fig. 2B). Next, we validated the observed changes in *circHomer1* expression after 3-day and 7d-day MD from our screens via RT-qPCR, along with several mRNAs known to be regulated by MD. As expected after 3-day MD, *Bdnf* and *Nptx2* were downregulated in contralateral V1(19). *Homer1a* mRNA was also significantly downregulated after 3-day MD, in contrast to *circHomer1*, validating the dissociation between *Homer1a* and *circHomer1* levels after 3-day MD (Fig. 2C, left). After 7-day MD, a regulator of homeostatic synaptic plasticity, *Stat1*(22), was upregulated in contralateral V1 compared to ipsilateral V1 (Fig. 2C, right), validating a previous marker of prolonged MD(15, 19, 22). We also saw that the expression of *circHomer1* was significantly decreased after 7-day MD along with a further decrease in *Homer1a* (Fig. 2C). These results suggest that *circHomer1* has a role in MD induced plasticity distinct from *Homer1a*.

Expression of many mRNAs involved in activity-dependent plasticity peak during the critical period. To determine the developmental expression profiles of *Homer1a* and *circHomer1* over the mouse's lifespan, we measured their expression in V1 at various time points using RT-qPCR. *circHomer1* expression increased significantly starting at ~P24, aligning to the start of the critical period (Fig. 2D, left), while *Homer1a* expression did not increase until P60, past the close of the critical period (Fig. 2D, middle). *circHomer1* expression appeared to plateau at P60 and remained at similar levels of expression in mice as old as 1.5 years. Expression of another circRNA, *circTulp4*, did not change across development or adulthood indicating that the developmental expression profile of *circHomer1* is not a shared feature of all circRNAs (Fig. 2D, right). These data show that the start of *circHomer1*-specific biogenesis parallels a period of activity-dependent synaptic maturation during development, further suggesting a functional role of *circHomer1* in developmental plasticity.

***circHomer1*-depletion delays ocular dominance plasticity**

The regulation of *circHomer1* expression by MD and the peak in *circHomer1* expression at the start of the critical period mirrors that of mRNAs with known roles in synaptic plasticity. To determine if *circHomer1* has a role in ocular dominance plasticity, we used a short hairpin RNA (shRNA)-mediated depletion strategy targeting the backsplice junction of *circHomer1*, which has been previously validated *in vivo* to specifically downregulate *circHomer1* in the cortex(7). Lentiviral transduction of the shRNA resulted in a close to 2-fold, significant reduction of *circHomer1* RNA with no changes in total *Homer1* mRNA expression (Supplementary Fig. 2A). sh-*circHomer1* also had no effect on *Homer1a* and total *Homer1* protein levels (Supplementary Fig. 2B).

To examine the effects of *circHomer1* depletion on ocular dominance plasticity, we quantified eye-specific responses in the binocular zone of V1 by using optical imaging of intrinsic hemodynamic signals measured before and after 3-day or 7-day MD. We then compared results between mice injected with a sh-scramble (control) or sh-*circHomer1* virus (Fig. 3A). Visual responses in V1 were robustly elicited *in vivo* following *circHomer1* depletion (Fig. 3B), indicating that functional visual drive and retinotopic mapping persists in sh-*circHomer1* animals. To compare the visual drive elicited by the

two eyes in V1, the normalized difference between contralateral (closed-eye) and ipsilateral (open-eye) responses during optical imaging was measured to determine the ocular dominance index (ODI). Change in ODI following MD was then used as a measure of cortical plasticity(23).

In the preMD condition, there was no difference in ODI between sh-scramble and sh-circHomer1 mice. After 3-day MD, the ODI of sh-scramble mice decreased significantly as expected. In contrast, the ODI of sh-circHomer1 mice were unchanged after 3-day MD (Fig. 3C). After 7-day MD, however, the ODI of sh-circHomer1 mice were significantly decreased and not significantly different than sh-scramble mice (Fig. 3C).

We next examined the responses driven by the contralateral and ipsilateral eyes separately. Unlike in the sh-scramble mice, contralateral closed-eye responses of sh-circHomer1 mice did not decrease after 3-day MD. Similarly, ipsilateral open-eye responses were already significantly increased in sh-scramble animals after 3-day MD whereas they were moderately reduced in sh-circHomer1 animals (Fig. 3D). Despite the differences after 3-day MD, by 7-day MD in the sh-circHomer1 mice both contralateral and ipsilateral responses were comparable to the sh-scramble mice (Fig. 3D). Thus, the effects of *circHomer1* depletion are consistent with its regulation by MD: plasticity is impaired at 3-day MD when *circHomer1* expression is normally increased but not at 7-day MD when *circHomer1* expression is normally decreased.

***circHomer1* regulates dendritic spine morphology**

MD induces rapid remodeling of the dendritic spines of layer 2/3 V1 neurons, with 3-day MD significantly decreasing average spine volumes(8). As we had found that *circHomer1* was required for closed eye depression at 3-day MD and depletion of *circHomer1* blocked the effects (Fig. 3), we hypothesized that depletion of *circHomer1* would likewise impair MD-induced spine shrinkage. We injected an AAV expressing both RFP and sh-circHomer1 or sh-scramble shRNA into the binocular region of V1 at P15, prior to the start of the critical period. We also injected AAV9-hSyn-DIO-EGFP and AAV9-CaMKIIa-Cre virus in order to sparsely label neurons with GFP and quantified spine morphology of labeled V1 neurons from mice that had undergone no MD, 3-day

MD, or 7-day MD. To achieve a more detailed analysis of the dendritic spine structure than possible with traditional confocal imaging, we used epitope-preserving magnified analysis of the proteome (eMAP) to expand our tissue samples (Fig. 4A). The apical dendrites of V1 layer 2/3 pyramidal neurons expressing both GFP and RFP were selected for further analysis (Fig. 4B, left). Based on their morphology, dendritic spines were classified into four categories: mushroom, stubby, thin, and filopodia using standard criteria (Fig. 4B-C)(24).

In mice that did not undergo MD (No MD), sh-circHomer1 led to a significant drop in the density and percentage of mature mushroom spines(25), but not immature spines (stubby, thin and filopodia)(25) (Fig. 4D-E). After 3-day MD, as expected there was a significant decrease in the density and percentage of mature mushroom spines in sh-scramble mice when compared to the No MD condition. Conversely, the density of both mature and immature spines remained unchanged after 3-day MD in the sh-circHomer1 mice. After 7-day MD, in the sh-scramble mice the density and percentage of mature spines remained lower compared to the No MD condition, while the density of immature spines showed a significant increase. Mature and immature spine density in sh-circHomer1 mice after 7-day MD remained unchanged, but was no longer significantly different than in the sh-scramble mice (Fig. 4D-E).

As binary spine classification could obscure more subtle changes in the dendritic spines of sh-circHomer1 neurons, we also analyzed the average spine volume by performing 3D reconstruction. sh-circHomer1 led to a more than 50% decrease in average spine volume in the No MD condition (Fig. 4F, Supplementary Fig. 3A). After 3-day MD, the average spine volume decreased by more than 70% in sh-scramble mice compared to the No MD condition. In contrast, 3-day MD did not significantly alter spine volume in sh-circHomer1 mice (Fig. 4F-G, Supplementary Fig. 3B). After 7-day MD, spine volume was still significantly decreased in sh-scramble mice compared to the No MD condition, and while the sh-circHomer1 spine volume remained unchanged, the sh-scramble and sh-circHomer1 spine volumes were not significantly different (Fig. 4F, Supplementary Fig. 3C). Taken together, our findings suggest that *circHomer1* plays a crucial role in regulating the structural morphology of dendritic spines during short-term MD, which is putatively critical for driving closed eye depression.

Considering the effects *circHomer1* depletion had on the morphology of synapses, we sought to determine how this depletion affected the electrophysiological properties of neurons at basal conditions. We used whole-cell patch clamp recordings in acute slices from P28-33 mice to measure passive membrane and synaptic properties of layer 2/3 neurons infected with sh-*circHomer1* or sh-scramble. We did not find any difference in neuronal excitability (Supplementary Fig. 4), and only a slight decrease in miniature excitatory postsynaptic currents (mEPSC) frequency (Supplementary Fig. 5), consistent with a decrease in protrusion density(26). Based on these findings, we surmise that the observed deficits in 3-day MD closed eye depression and spine shrinkage following *circHomer1*-depletion is due to impaired activity-dependent plasticity as opposed to baseline synaptic deficits or occlusion.

***circHomer1* controls surface AMPA receptor expression**

The major mechanism underlying both reduced closed-eye drive and spine shrinkage following MD is a reduction in surface AMPA receptors(22, 23, 27). Therefore, we investigated the role of *circHomer1* in regulating surface AMPA receptor trafficking following MD using a biotinylation assay of the AMPA receptor subunit, GluA1 (Fig. 5A,B). As expected, 3-day MD led to a significant reduction of surface GluA1 compared to No MD. However, there was no reduction of GluA1 levels after 3-day MD in sh-*circHomer1* mice (Fig 5B, right). By 7-day MD, however, there was no significant difference in surface GluA1 expression between sh-scramble and sh-*circHomer1* mice. Based on these results, we hypothesized that *circHomer1* was necessary for activity-dependent AMPA receptor endocytosis. To examine this further, we treated primary neurons with bicuculline, a GABA_AR antagonist, to induce activity-dependent AMPA receptor internalization(28). 1- or 2-day treatment with bicuculline induced upregulation of *circHomer1* in neurons (Supplementary Fig. 6A), and *circHomer1*-depletion impaired bicuculline induced endocytosis of surface AMPA receptors labeled via SEP-GluA1 (Supplementary Fig. 6B,C). These data demonstrate that *circHomer1* depletion prevents 3-day MD-associated changes in surface GluA1 expression levels, thus indicating a potential functional mechanism for the disrupted ocular dominance plasticity after 3-day MD.

How might a non-coding circRNA contribute to AMPA receptor endocytosis? One possibility, given the previous observation of dendritically localized *circHomer1*(29), is through regulating other dendritic RNAs. The activity-regulated cytoskeleton-associated protein (Arc) is an immediate early gene product that has been shown to play a critical role in AMPA receptor endocytosis(28, 30), and *Arc* mRNA is trafficked to dendrites and translated locally in response to synaptic activity. We therefore tested whether Arc protein expression at dendritic spines is affected by *circHomer1* depletion following MD. We injected AAV9 expressing either sh-scramble or sh-*circHomer1* along with RFP, and sparsely labeled neurons in V1 with GFP as described in Figure 4. After processing the tissue with eMAP, postsynaptic Arc protein was labeled by immunostaining, and pyramidal neurons in layer 2/3 of V1 were selected for analysis. Next, we performed 3D reconstruction of the imaged dendrites (Fig. 5C), and quantified the volume of each Arc puncta expressed at dendritic spines. Intriguingly, the fraction of Arc-containing spines and the volume of Arc puncta increased significantly after 3- and 7-day MD in both sh-scramble and sh-*circHomer1* mice as compared to their No MD conditions (Fig. 5E,F). However, the mean volume of Arc puncta and the Arc volume/spine volume ratio in sh-*circHomer1* neurons was significantly smaller than that in sh-scramble neurons after 3-day MD (Fig. 5F,G). There was no difference in the mean volume of Arc puncta and the Arc volume/spine volume ratio between sh-scramble and sh-*circHomer1* neurons at 7-day MD. This is consistent with the impairment of surface GluA1 removal and spine shrinkage after 3-day MD in sh-*circHomer1* mice as compared to control (Figs. 4D-G, 5B). Together, these results demonstrate that *circHomer1*-depletion impairs GluA1 internalization following 3-day MD, which may be explained by *circHomer1*-depletion reducing the quantity of Arc protein accumulating at dendritic spines in response to MD.

Discussion

Despite the fact that circRNAs are abundantly expressed in mammalian brains and are preferentially derived from genes encoding synaptic proteins(29, 31), it was unclear if circRNAs have any role in regulating synaptic plasticity or function. Using an *in vivo* circular-transcriptome analysis, we identified several promising plasticity-associated circRNAs with differential expression in binocular V1 following 3-day MD in critical period age mice. We focused on *circHomer1*, a circRNA derived from the *Homer1* gene which encodes important synaptic scaffolding proteins and an activity dependent linear isoform, *Homer1a*, which is a key regulator of glutamatergic synaptic signaling(32).

circHomer1 and *Homer1a* were differentially regulated by 3-day MD, but in opposing directions with the expression level of *circHomer1* increasing and that of *Homer1a* decreasing following short-term MD. Following longer term, 7-day MD, however, expression levels of both *circHomer1* and *Homer1a* declined. The developmental expression of *circHomer1* increased rapidly in V1 between P15 and P28, the early part of the critical period for ocular dominance plasticity, which in combination with its differential expression following 3-day MD strongly suggested a role for *circHomer1* in such plasticity. Indeed, loss of *circHomer1* disrupted ocular dominance plasticity following 3-day, but not 7-day, MD without effecting baseline visual responses. Depletion of *circHomer1* led to less mature dendritic spines, and impaired experience-dependent changes in spine morphology and volume following MD.

Homer1 proteins have been suggested to play critical roles in regulating synapse development, synaptic strength, and homeostatic synaptic scaling(33–37). At the postsynaptic density, the activity-dependent short protein isoform of the gene, *Homer1a*, has dominant-negative effects on the constitutive longer forms of Homer1 (*Homer1b/c*), and through this interaction regulates the clustering of mGluRs(34–36) and mGluR-dependent NMDA and AMPA receptor currents(34, 38–41). It is intriguing to theorize that *circHomer1* could have a similar dominant negative affect as its linear, activity-dependent counterpart, and *circHomer1* may regulate synaptic *Homer1b/c* via such a mechanism (as discussed below(42)). However, there are key difference between *Homer1a* and *circHomer1* that cast doubt on this shared mechanism. In contrast to the upregulation of *circHomer1*, *Homer1a* is reduced following 3-day MD (Fig. 2C), and

depletion of *Homer1a* does not affect the 3-day shift in ocular dominance plasticity and reduction of closed-eye responses as a result of MD(43). *Homer1a* depletion also alters the establishment of contralateral bias of V1 responses under basal conditions, which is not affected by *circHomer1* depletion (Fig. 3C,D). Thus, although both *Homer1a* and *circHomer1* are regulators of cortical plasticity, they serve different roles in the expression of experience-dependent plasticity.

It remains unclear how neuronal activity regulates *circHomer1* expression, as the only demonstrated precursor of *circHomer1* is non-activity dependent *Homer1b* mRNA(44). Given that *Homer1a* contains the relevant regions to form *circHomer1*, including a section of intron 5(44), it is plausible that *circHomer1* could derive from *Homer1a*, allowing its expression to change in tandem with *Homer1a* transcription. However, during MD and development *in vivo* and bicuculline treatment *in vitro*, we observed timepoints where changes in *circHomer1* expression appear decoupled from or even opposing changes in *Homer1a*. Circular RNA species decay more slowly than their linear counterparts(45) and changes in transcription thus tend to result in larger, longer relative increases in circRNA levels(46), but this seems insufficient to explain this discrepancy. More plausible, perhaps, is that the rate of *Homer1* circularization is itself regulated by activity(44).

Thus, we asked whether a constant circularization rate of *Homer1b* and *Homer1a*, a variable circularization rate of *Homer1b*, or a variable circularization rate of *Homer1b* and *Homer1a* best fit our observed data (Supplementary Fig. 7). Our models shows that across multiple paradigms, a constant circularization rate of *Homer1a* and *1b* or a variable circularization rate of *Homer1b* alone is insufficient to explain the observed expression levels of *circHomer1*. Instead, our data are best fit when adding a variable, activity-dependent circularization rate of *Homer1b* and *Homer1a*. In this way, *circHomer1* levels can increase when *Homer1a* levels do not change or even decrease; importantly, the model accounts for the bidirectional change in *circHomer1* after 3-day vs 7-day MD. (Fig. 2C-D, Supplementary Fig. 7A). Such regulation could be facilitated by recently described molecular pathways underlying *circHomer1* biogenesis(44) or by changes in other *Homer1* mRNA products not measured in our experiments (for instance, *Homer1b*(42)). Future work is needed to determine if *Homer1a* can indeed

give rise to *circHomer1*, whether circularization meaningfully decreases linear mRNA availability, and if circular RNA decay rate is static or itself regulated by activity.

The mechanism(s) of circRNA function are an area of active investigation. circRNAs are enriched in neurons and are believed to play critical roles in regulating neuronal development and synaptic plasticity(7, 29, 47). From within the top 100 candidates identified in our MD RNAseq screen, several circRNAs were already reported in the literature to have biological functions in other contexts(48–50). These include the neuronally-enriched circRNA *Cdr1as* (also known as ciRS-7), which has been found to contain a large number of binding sites for miR-7, a regulator of neurodevelopment(5, 51–54). This enrichment for miR-7 binding sites effectively serves as a “miRNA sponge”, and *Cdr1as* knockout mice exhibit behavioral deficits and altered neuronal electrophysiological properties(5, 6).

An important conclusion of our study is that *circHomer1* has a critical role in the reduction of synaptic drive that accompanies the initiation of MD. Specifically, we found that *circHomer1* regulates surface GluA1 levels and Arc protein expression at dendritic spines. However, the exact mechanism of this regulation warrants further investigation. Previous studies suggest that *circHomer1* regulates alternative splicing of mRNA isoforms(7) as well as synaptic expression of *Homer1b* mRNA in the orbitofrontal cortex via direction competition for HuD binding(42). It remains to be elucidated whether these mechanisms also contribute to the function of *circHomer1* in visual cortical plasticity. Additionally, in silico analysis predicts that *circHomer1* interacts with RNA binding proteins (RBPs), such as FMRP and FUS(55) (Supplementary Table 5). FMRP and FUS are key regulators of synaptic plasticity(56, 57), involved in modulating the dendritic transport and translation of synaptic plasticity-related mRNAs. Both FMRP and FUS localize to the neuronal RNA transport granules carried by the motor protein KIF5 in dendrites(58). These neuronal RNA transport granules transport *Arc* mRNA from the soma to distal dendrites(58). It is possible that during 3-day MD, increased *circHomer1* expression modulates dendritic transport of neuronal RNA transport granules to impact localization or availability of key-plasticity related mRNAs, such as *Arc*. We therefore propose that the interaction between *circHomer1* and RBPs promotes the dendritic

expression or targeting of *Arc* mRNA, and as a result regulates the activity-dependent expression of Arc protein, driving AMPA receptor internalization and spine shrinkage.

This study identified tens of circRNAs differentially expressed following experience-dependent plasticity and highlights *circHomer1*, a neuron-enriched circRNA derived from the Homer1 gene, as a critical regulator of V1 plasticity during the critical period. Our findings advance the understanding of circRNA regulation during experience-dependent plasticity and shed light on their functional significance in developmental processes.

Acknowledgments

We thank Jamie Benoit for his contribution to the initial RNA-seq experiment. We thank Taylor Johns, Austin Sullins and other members of the Sur lab and the Ip lab for their help and support. We thank Hovy Wong for comments on the manuscript. We thank Lorena Rubino for her assistance in analyzing RNA-seq data. We thank Cara Kwong for her technical assistance in neuronal cultures. We thank the MIT BioMicroCenter for running the RNA-seq library preparation and sequencing. We thank scidraw.io for the schematic, licensed under a Creative Commons 4.0 license (<https://creativecommons.org/licenses/by/4.0/>). This work was supported by NIH grants R01MH085802 (M.S.), R01EY028219 (M.S.), F31EY033649 (K.T.), F32EY032756 (K.J.), the Simons Foundation Autism Research Initiative through the Simons Center for the Social Brain, MIT (M.S.), the National Research Foundation of Korea (RS-2023-00264980; T.K.), the Hong Kong Research Grants Council Early Career Scheme (24117220; J.I), General Research Fund (14117221; J.I.), Area of Excellence Scheme (AoE/M-604/16; J.I., A.F.), Theme-based Research Scheme (T13-605/18-W; J.I., A.F.), Lo Kwee-Seong Biomedical Research Fund (J.I.), Faculty Innovation Awards from the Faculty of Medicine CUHK (FIA2020/A/04; J.I.), and NARSAD Young Investigator Grant from the Brain & Behavior Research Foundation (J.I.).

Author Contributions

J.I., N.M., M.N., M.S., K.J. conceived experiments with input from others. M.N., C.D. and S.Y. performed the cortical dissections and RNA and protein purifications. C.D., M.N. and Y.Z. analyzed RNA-seq data. M.N., Y.C. and C.D. performed qPCR experiments. K.J., K.T., J.Z. and J.I. performed surgeries and viral injection, and carried out *in vivo* optical imaging experiments. K.L. analyzed optical imaging data. Y.C., S. Y. and J.Z. performed spine morphology analysis. K.J., K.T. and C.Z. performed ExFISH experiments with input from E.B.. Y.C., S.Y., T. K., D. Y. and J.I. performed eMAP experiments with inputs from K.C. J.I. performed the surface biotinylation assay and protein analyses. J.S. performed electrophysiological recordings and analyses. Y.C., Y.W., Y.D. performed neuronal culture experiments and relevant analyses. A.F. provided expertise on neuronal culture experiments. N.M. shared the sh-RNA

constructs. G.H. performed the modeling of RNA expression. K.J., J.I., and M.S. contributed to analysis of experiments and interpretation of results. J.I., K.J. and M.S. wrote the manuscript with input from others. All authors edited the manuscript.

Competing Interest Statement

N.M. is CSO of Circular Genomics Inc, Albuquerque, NM.

Data, Materials, and Software Availability

All RNA sequencing data have been deposited in GEO. The code will be made available upon reasonable request.

Materials and Methods

Animals

Experiments were carried out in mice under protocols conforming to NIH guidelines and approved by MIT's Animal Care and Use Committee or by CUHK's Animal Experimentation Ethics Committee. Wildtype C57BL/6J mice (JAX000664) were sourced from Jackson Laboratory or CUHK's Laboratory Animal Services Centre. Mice were group-housed whenever possible with up to 5 same-sex mice per cage. The cages were in a standard animal facility room with a 12-hour/12-hour light/dark cycle. Food and water were available ad libitum. Both male and female mice were used for experiments.

Eyelid suture and monocular deprivation

For monocular deprivation experiments, mice were anesthetized using 2-3% isoflurane. The top and bottom eyelid of the right eye was trimmed, and sterile nylon sutures (7-0) were used to suture the eyelid, which were further sealed with Vetbond (3M). The suture was inspected for the next 3-7 days post-closure to ensure that the eye did not reopen. Mice that exhibited incomplete eyelid closure were removed from the experiment.

circHomer1 depletion via shRNA and validation

For *circHomer1* depletion experiments, the following viruses were used: lentivirus expressing pLV-mU6-scrambled-shRNA::SYN-tdTomato or pLV-mU6-*circHomer1a*-shRNA::SYN-tdTomato (1.2×10^9 IFU/mL, System Biosciences) (gift from N. Mellios), or AAV9 expressing pAV-U6-sh-scramble-CMV-DsRed or pAV-U6-sh-*circHomer1*-CMV-DsRed (2×10^{13} vg/mL, Vigene). For the *in vivo* shRNA experiments, binocular V1 in the left hemisphere of P15 pups was targeted. Briefly, sh-scrambled or sh-*circHomer1* viruses were loaded into a pulled-glass micropipette with a beveled tip, lowered into L2/3, and virus was infused at a rate of 100 nL/min. The following coordinates were used (in mm from lambda at P15): AP: -2.0 to -1.0; ML: -2.8, DV :-0.45 to -0.2. A minimum of 10 days was allowed for viral transduction and sufficient expression of the constructs in all experiments. To estimate the efficiency and specificity of sh-*circHomer1*

after virus injection, the mouse brain was examined using a dual fluorescent protein flashlight (Nightsea) after mouse sacrifice and dissection. The tissue expressing RFP was dissected for RNA purification for RT-qPCR (see below), and protein isolation for Western blot. For protein isolation, the RFP-expressing tissue were homogenized in RIPA buffer (1% NP40, 0.1% SDS and 0.5% sodium deoxycholate in PBS). The homogenate was centrifuged at 14,000 x g for 15 min and the supernatant was collected. Protein concentration was measured by BCA protein assay, and 20 µg total protein lysate was boiled for 5 min with 6x loading buffer. Standard Western blot was performed. Antibodies used include Homer1 (160003; Synaptic Systems), Homer1a (160013; Synaptic Systems), and α -Tubulin (sc32293; Santa Cruz).

RNA Sample Preparation

RNA was extracted from fresh tissue. Tissue for RNA extraction was isolated from V1 contralateral and ipsilateral to the sutured eye after 3-day MD (at P28), 7-day MD (at P32) or from mice that had not undergone MD (various ages based on experiment). Briefly, mice were anesthetized with isoflurane and transcardially perfused with ice-cold phosphate buffered saline (PBS) for at least 5 min. A sterile scalpel blade and forceps were used to surgically micro-dissect the appropriate tissue section. The dissected tissue was immediately placed into a 2-mL lysing tube containing 1.4 mm spherical ceramic beads (MPBio, Lysing Matrix D, Cat. No. 116913050) and pre-filled with 1 mL of ice-cold TRIzol (Ambion, Cat. No. 15596-026) and then immediately homogenized with a bead-based homogenizer (FastPrep-24 5G, MPBio) using the preset settings for mouse brain tissue (8.0 m/sec, 30 sec). Once foaming has subsided at room temperature, the homogenate was transferred into 2 mL Phase Lock Tube (Heavy; 5Prime Bio, Cat. No. 2302830) pre-filled with 200 µL chloroform and briefly vortexed. Samples were centrifuged at 12,000 x g for 10 min at 2-4°C. The colorless upper aqueous layer was then transferred into a new 2.0 mL LoBind tube that was pre-filled with 1.5 volumes of 100% EtOH (~600 µL), then mixed thoroughly by pipetting up and down several times, and then briefly centrifuged. The sample was further purified using Zymo RNA Clean & Concentrator-5 (Zymo Research, R1016) according to the manufacturer's recommended protocol and always performed with the optional in-

column DNase I treatment. RNA was eluted twice with $\geq 6 \mu\text{L}$ 1x TE buffer (pH 7.5). The approximate concentration and relative purity of RNA was determined using a NanoDrop 2000 spectrophotometer (Thermo Scientific). The purified RNA was either immediately used for downstream applications (i.e., reverse transcription) or stored at -80°C .

RNA sequencing library preparation

For samples to be sequenced, RNA quality was assessed using AATI Fragment Analyzer. Samples with RNA Quality Number of >8.0 were further processed. Indexed cDNA libraries were generated using the SMARTer Stranded Total RNA-Seq Kit v2 and multiplexed sequencing was performed on Illumina HiSeq 2000 or Novaseq 6000.

RNAseq Analysis

For the mRNA sequencing, read alignment was performed using HISAT2(59). Fragment counts were obtained using featureCounts(60). Differential expression analysis was performed using DESeq2(61). For the circRNA sequencing, reads were aligned and fragment counts were obtained using circTools(20). Fragment counts were obtained using the Cufflinks pipeline(62). Differential expression analysis was performed using the Bioconductor package Limma(63). Gene Ontology enrichment analysis was performed using the Bioconductor package clusterProfiler(64). Differential expression analysis of 3-day MD RNAseq data was performed comparing the contralateral side and ipsilateral side within animal. For 7-day MD RNAseq, differential expression analysis was performed comparing control, no MD animals and MD animals (contralateral side).

cDNA Preparation for qPCR

Total RNA was reverse transcribed using SuperScript IV VILO with ezDNase treatment (Thermo Fisher, Cat. No. 11766050) according to manufacturer's recommended protocol with the following modifications: the maximum input of total RNA was lowered to $2 \mu\text{g}$ per $20 \mu\text{L}$ reaction, ezDNase digestion was extended to 5 min, and reverse transcription temperature was increased to 55°C . After the RT reaction, cDNA was diluted with 1x TE buffer (pH 8.0).

qPCR Analysis

Applied Biosystems QuantStudio 3 Fast thermocycler was used for all qPCR amplification and detection in this study. PowerUp SYBR Green Master Mix (Applied Biosystems, Cat. No. A25742) was used according to the manufacturer's recommended protocol. Primers used were listed in Supplementary Table 6. Mouse *Gapdh* was used as the internal control for normalization. For the fold change calculation, the $\Delta\Delta Cq$ method was used.

Expansion FISH (ExFISH)

The ExFISH protocol was performed as previously described(21, 65). In brief, AAV5-phSyn1(S)-tdTomato-WPRE (Addgene) was injected into L2/3 of mouse binocular V1 to label neurons. The brain was perfused with ice-cold PBS and 4% PFA, fixed overnight in 4% PFA, and then 80 μ m slices from the visual cortex were stored in 70% ethanol. Slices expressing tdTomato were trimmed to the area containing tdTomato positive neurons, rehydrated in PBS, and incubated with LabelX in MOPS buffer overnight at 37°C. Slices were then gelled with StockX solution and digested with proteinase K overnight at 37°C. After digestion, the slices were expanded in 0.05X SSCT and subjected to HCR-FISH hybridization for *circHomer1* following the standard protocol (<http://molecularinstruments.org>). After hybridization, slices were re-expanded in 0.05x SSCT to ~3.5x of their original size for imaging. Post-expansion confocal imaging of expanded brain tissue was performed on an Andor spinning disk confocal system (CSU-W1 Yokogawa) with a 40x 1.15 NA water objective on a Nikon Ti-E microscope body.

Optical imaging of intrinsic signals

At postnatal day P15, sh-scramble or sh-circHomer1 vectors were injected into left binocular V1 as described above, and at P22 a 3 mm craniotomy was performed over the same area, where a 5 mm diameter glass window stacked on top of a 3 mm diameter glass window was fitted over the craniotomy with dental cement, together with a metal headplate. Baseline optical imaging was performed at P25, prior to MD. MD lasted either 3 days or 7 days, after which sutures were removed and the closed eye

was reopened under isoflurane anesthesia before optical imaging experiments to assess the effects of 3-day or 7-day MD on V1 responses. Optical imaging was performed as previously described(23). Briefly, mice were lightly anesthetized with isoflurane (0.5-1%), the window was cleaned with 70% ethanol and a cotton tipped applicator, and the headplate was attached to the imaging rig to minimize head movements. Green light (560 nm) was used to focus 400 μm below the cortical surface. Red light (630 nm) was used for functional imaging, and the change in reflectance was captured by an electron multiplying CCD camera (Cascade 512B; Roper Scientific) during the presentation of visual stimuli.

Visual stimulation and optical imaging analysis

The visual stimulus was a horizontal bar 30° wide, made of flickering checkerboard over a black background, drifting continuously through the peripheral–central dimension of the visual field. After moving to the last position, the bar would jump back to the initial position and start another cycle of movement; therefore, the chosen region of visual space (72° x 72°) was stimulated in a periodic manner (12 s/cycle, 20 repetitions). Images were continuously captured at the rate of 30 frames/s during each stimulus session of 4 min, with a separate stimulus session for each of the 4 cardinal directions. A temporal component at the stimulus frequency (12s⁻¹) was calculated pixel by pixel from the whole set of images using custom python scripts (https://github.com/Palpatineli/oi_analyzer). The amplitude of the FFT component was used to measure the strength of visually driven response for each eye, and the ODI was derived from the response (R) of each eye at each pixel as $\text{ODI} = (R_{\text{contralateral}} - R_{\text{ipsilateral}})/(R_{\text{contralateral}} + R_{\text{ipsilateral}})$. The binocular zone was defined as the cortical region that was driven by both eyes. The response amplitude for each eye was defined as fractional changes in reflectance over baseline reflectance ($\Delta R/R \times 10^{-3}$), and the top 50% pixels were analyzed to avoid background contamination.

Epitope-preserving magnified analysis of the proteome (eMAP)

Mice were injected at P15 (from lambda at P15: AP: -2.0 to -1.0; ML: -2.8, DV :-0.45 to -0.2) with AAV2/9-hSyn-DIO-EGFP (1×10^{13} vg/mL), AAV2/9-CaMKIIa-Cre (5×10^8 vg/mL)

and AAV9 expressing either pAV-U6-sh-scramble-CMV-DsRed or pAV-U6-sh-circHomer1-CMV-DsRed (1×10^{13} vg/mL). Animals were allowed to express virus for a minimum of 10 days before MD. After MD, mice were transcardially perfused under deep anesthesia with ice-cold PBS followed by ice-cold 4% PFA (in PBS), and then brains were post-fixed in 4% PFA at 4°C overnight. eMAP processing was performed following protocols previously described(66, 67). Tissue embedding was performed using eMAP solution (30% acrylamide, 10% sodium acrylate, 0.1% bisacrylamide, 0.03% VA-044 in PBS) under vacuum, following hydration using hydration solution (0.02% sodium azide in PBS) and sectioning into 60um thick using Leica VT1000S vibratome. Tissue clearing was performed by incubation in clearing solution (6% SDS, 0.1 M phosphate buffer, 50 mM sodium sulfite, 0.02% sodium azide in DI water, pH 7.4) at 37°C for 4 hours. If applicable, after washing with PBST (0.1% Triton X-100, 0.02% sodium azide in PBS), samples were stained with primary antibodies against GFP (A10262, Invitrogen) and Arc (156003, Synaptic Systems) diluted in PBST at 37°C for 48 hours. After washing with PBST, samples were stained with secondary antibodies diluted in PBST for 48 hours. Expansion was performed using 0.01x PBS before imaging. Approximately 3x total linear expansion was achieved consistently. Pyramidal neurons in V1 which were double-positive for RFP and GFP were identified and imaged using Leica SP8 confocal microscope with 20x 0.75 NA or 63x 1.2 NA water immersion lens.

Spine morphology and Arc puncta volume analysis

Dendrites and dendritic spines for analysis were selected and analyzed by an experimenter blinded to experiment condition. To analyze dendritic spine morphology, the length (L), head width (H) and neck width (N) were measured by ImageJ. Dendritic spines were classified into 4 types according to the criteria previously described(24). Briefly, the average length of spine head in the No MD sh-scramble group (\bar{H}) was calculated. Protrusions with $H > N$ and $H > \bar{H}$ were defined as mushroom spines; protrusions with $H > N$ and $H < \bar{H}$ were defined as thin spines; protrusions with $H \leq N$ and $L < \bar{H}$ were defined as stubby spines, and protrusions with $H \leq N$ and $L > 1.5 * \bar{H}$ were defined as filopodia. For dendritic spine volume and surface area analysis, 3D

reconstruction and quantification of dendritic spines volume was performed using the “Filament” function in Imaris software. The analysis of Arc puncta volume was performed using the “Surface” function in Imaris, and only the Arc puncta located at dendritic spines were selected for quantification. The raw data was then divided by 3^3 (=27) to convert to values that closely approximates the unexpanded volume.

Preparation of acute brain slices for electrophysiology

Mice injected with either sh-scramble or sh-circHomer1 lentivirus (as described above) were anesthetized with 2-3% isoflurane and decapitated. Brains were rapidly removed and placed into ice-cold low-Ca²⁺, low-Na⁺ sucrose cutting solution consisting of (in mM): 234 sucrose, 11 glucose, 24 NaHCO₃, 2.5 KCl, 1.25 NaH₂PO₄, 10 MgSO₄, and 0.5 CaCl₂. Cutting solution was oxygenated with a mixture of 95% O₂ and 5% CO₂. 300µm slices were cut in a coronal orientation using a vibratome (Leica Biosystems, Buffalo Grove, IL) and placed into a recovery chamber filled with oxygenated ACSF consisting of (in mM): 126 NaCl, 2.5 KCl, 1.25 NaH₂PO₄, 1 MgSO₄, 2 CaCl₂, 10 glucose, 26 NaHCO₃. Slices were allowed to recover at 34°C for 1 hour before being kept at room temperature (25°C) for the remainder of the experiment.

Current clamp recordings and analysis

TdTomato-positive neurons were identified in Layer 2/3 of the V1 binocular region. Recordings were made at 34°C in ACSF containing 10 µM CPP, 20 µM DNQX, and 10 µM SR95531 to isolate passive membrane properties. Signals were collected at 10kHz using a Multiclamp 700B amplifier and digitized using a Digidata 1440A (Molecular Devices, San Jose, CA). Whole-cell patch clamp recordings were made using borosilicate glass electrode with an open-tip resistance of 2-5 MΩ filled with an intracellular solution consisting of (in mM): 130 potassium gluconate, 10 HEPES, 5 KCl, 5 EGTA, 2 NaCl, 1 MgCl₂, 10 TEA-Cl, 10 phosphocreatine, 2 Mg-ATP, 0.3 Na-GTP (pH adjusted to 7.28, osmolarity adjusted to 290 mOsm). Current steps of 250 ms duration were applied, from -100 pA increasing to 650 pA at 25 pA increments. The holding current was returned to 0 pA for 750 ms between each current injection step. Ra (access resistance) and Rm (membrane resistance) were also measured in response to

a 5 mV depolarizing step, and membrane capacitance was calculated as $C = \frac{\tau}{R_m}$, where τ is the decay of the capacitive transient in response to the 5 mV step. Access resistance was monitored throughout the recording and recordings with >20% change in access resistance or had access resistance >30 M Ω were excluded.

mEPSC recordings and analysis

Slices were prepared as above. Recordings of tdTomato positive neurons were made at 34°C in ACSF containing 10 μ M CPP, 10 μ M SR95531, and 1 μ M tetrodotoxin to isolate miniature AMPA receptor-mediated currents. Signals were collected at 10kHz and filtered at 2kHz using a Multiclamp 700B amplifier and digitized using a Digidata 1440A (Molecular Devices, San Jose, CA). Whole-cell patch clamp recordings were established using borosilicate glass electrode with an open-tip resistance of 2-5 M Ω filled with an intracellular solution consisting of (in mM): 100 potassium gluconate, 10 HEPES, 20 KCl, 0.5 EGTA, 10 NaCl, 8 phosphocreatine, 2 Mg-ATP, 0.3 Na-GTP (pH adjusted to 7.23, osmolarity adjusted to 290 mOsm). Neurons were voltage-clamped at -70 mV and stable gap free recordings were made for at least 2 minutes. Access resistance was monitored throughout the recording and recordings with >20% change in access resistance or had access resistance >30 M Ω were excluded. mEPSC events were detected using the MiniAnalysis software (Synaptosoft, Fort Lee, NJ).

Surface Protein Biotinylation Assay

For the measurement of surface proteins, we first prepared 300 μ m acute coronal slices containing V1 in ice-cold ACSF and then washed slices 3 times in ice-cold ACSF in 6-well plate on shaker. The sections were incubated in 100 μ M S-NHS-SS-biotin for 45 min (~1 mL per well). The superficial layers of V1 were dissected into a new 1.5 mL tube filled with ice-cold ACSF and homogenize in RIPA buffer. The homogenate was centrifuged at 14,000 x g for 5 min and the supernatant was transferred into a new 1.5 mL tube. ~20% volume was transferred into a new 1.5 mL tube and stored at -80°C to be used later as a total protein control. ACSF was added to the remaining supernatant for a final volume of 1 mL per sample. 40 μ L of streptavidin beads were added and incubated on a shaker overnight at 4°C. Samples were then centrifuged at 3,500 x g for

1 min. The supernatant was discarded and then the beads were washed 3x in 1:1 v/v ice-cold solution of ACSF and RIPA buffer. Then, 40 μ L of 2x loading buffer was added, mixed briefly, and boiled for 5 min. Standard Western blot was performed. Antibodies used include GluA1 (04-855, clone C3T; Millipore), and pan-Cadherin (ab6529; Abcam).

Neuronal cultures, transfection, and pharmacological treatment

Cultured primary rat hippocampal and cortical cells were prepared as previously described(68). In brief, Sprague–Dawley rat embryos were sacrificed on embryonic day 18. The hippocampus and cortices were dissected, and the cells were dissociated with trypsin. Hippocampal cells were cultured on 18-mm coverslips coated with 1 μ g/mL poly-D-lysine at 1×10^5 cells per coverslip in Neurobasal Plus medium supplemented with 2% B27 Plus and 0.5mM L-glutamate. Cortical cells were cultured on 60-mm cultural dishes coated with 100 μ g/mL poly-L-lysine at 3×10^6 per dish in Neurobasal medium supplemented with 2% B27 and 10mM glucose. All cells were maintained at 37 °C in a humidified atmosphere with 5% CO₂. The cortical neurons were treated with bicuculine (20 μ M) at DIV 13. Total RNA of cortical neurons was extracted at 0, 2, 6, 24, or 48 hours later using NucleoSpin RNA Mini kit (Macherey-Nagel, 740955) according to the manufacturer's protocol. The hippocampal neurons at DIV 11 were transfected with a *circHomer1* or scrambled control shRNA construct and SEP-GluA1 using calcium phosphate precipitation(68). The transfected neurons were then treated with bicuculine (20 μ M, 48 h) for subsequent morphological analysis. At DIV 19 the hippocampal neurons were fixed with 4% PFA, and blocking was performed for 1 hour at room temperature with 1% BSA in PBS. Antibody against GFP (A10262, Invitrogen) was diluted in 1% BSA in PBS and incubated with cells at 4°C overnight. After washing with PBS, the cells were incubated with secondary antibody for 1 hour at room temperature. The cells were then washed with PBS and mounting was performed. Imaging was performed under Leica SP8 confocal microscope using a 63x oil immersion lens with 1.4 numerical aperture.

Computational modeling

As it is unclear what stages in the biogenesis of *circHomer1* confer its activity-dependence, we compared three nested dynamical system models(69) of *circHomer1* expression with the same basic architecture to assess which best fit our data. We modeled three time-varying outputs: (1) *Homer1b* RNA levels (H1b), (2) *Homer1a* RNA levels (H1a), and (3) *circHomer1* RNA levels (CH). Dynamical changes in gene expression were described by the following differential equations:

$$\begin{aligned}\Delta H1a &= (H1aTR - decL \cdot H1a - H1aC \cdot CR \cdot H1a)dt \\ \Delta H1b &= (H1bTR - decL \cdot H1b - CR \cdot H1b)dt \\ \Delta CH &= (CR \cdot H1b + H1aC \cdot CR \cdot H1a - decCH \cdot CH)dt\end{aligned}$$

with H1a/bTR denoting transcription rates of pre-mRNA, decL denoting linear mRNA decay rate, decCH denoting circular RNA decay rate, CR denoting circularization rate, and H1aC denoting a logical operator of whether *Homer1a* can be circularized (1 if true, 0 if false). Parameters were fit separately for each model/experiment combination, but the fit parameter values for a particular model were largely consistent across experiments.

We hypothesized(42, 44) that the activity-dependence of *circHomer1* expression was most likely to arise from circularization of an activity-dependent mRNA (*Homer1a*) and/or activity dependent circularization of a constitutively expressed mRNA (*Homer1b*). The three models tested were as follows. (1) The constant circularization model fit a constant circularization rate of *Homer1a* and *Homer1b*, with the only time varying parameter being the transcription rate of *Homer1a* which was fit to measured data. (2) The variable circularization model allowed the circularization rate to vary over time, however only *Homer1b* could be circularized. (3) The third, full model also included time varying circularization but both *Homer1b* and *Homer1a* could be circularized. *Homer1a* and *circHomer1* levels were explicitly fit to minimize squared error from observed datapoints for each experiment. *Homer1b* levels were treated as a 'hidden' variable; as they were not measured experimentally and were not a part of model testing.

Models were initialized 10 days before the first timepoint to allow RNA levels to stabilize before permitting any changes in transcription or circularization. Because of the

varied measurements and methods across experiments, data in each model were normalized to the first timepoint, $T=0$. In models where circularization of *Homer1a* was permitted, the same circularization rate was applied to both *Homer1a* and *Homer1b* pools. Fit circularization rates were 1 to 2 orders of magnitude smaller than the linear transcription rates(70), and varied with activity by at most a factor of 4. In each of the models, the decay rate of *circHomer1* was constrained to be slower than that of linear *Homer1* by a factor of ≥ 2 (45). All models were run with 15 minute timesteps. *Homer1b* transcription rate, linear decay rate, and circular decay rate were fit as constant parameters in each model. *Homer1a* transcription rate was fit as a variable parameter in each model. Circularization rate was fit as a constant parameter in the constant circularization model, and a variable parameter in the variable circularization and full model. Fitting was performed and AIC scores for each model were computed using the python package `lmfit`.

Statistical analysis

Data are presented as mean \pm SEM in quantitative analysis unless other specified. When two independent experimental groups were analyzed, Student's t-test was performed, while paired t-test was performed when two paired experimental data were analyzed. When more than two independent experimental groups were analyzed, one-way ANOVA followed by Tukey post hoc test was performed. For those experiments exploring the effect of *circHomer1* during MD by *circHomer1* depletion, two-way ANOVA followed by Tukey post hoc test was performed. For optical imaging, mixed-effects model following Holm-Sidak multiple comparisons test was performed. For mEPSC quantification, two-sample Kolmogorov-Smirnoff test was performed. Statistical significance was defined as $p < 0.05$.

References

1. E. L. Yap, M. E. Greenberg, Activity-Regulated Transcription: Bridging the Gap between Neural Activity and Behavior. *Neuron* **100**, 330–348 (2018).
2. W. Chen, E. Schuman, Circular RNAs in Brain and Other Tissues: A Functional Enigma. *Trends Neurosci* **39**, 597–604 (2016).
3. L. Szabo, J. Salzman, Detecting circular RNAs: bioinformatic and experimental challenges. *Nat Rev Genet* **17**, 679–692 (2016).
4. L. L. Chen, The expanding regulatory mechanisms and cellular functions of circular RNAs. *Nat Rev Mol Cell Biol* **21**, 475–490 (2020).
5. B. Kleaveland, C. Y. Shi, J. Stefano, D. P. Bartel, A Network of Noncoding Regulatory RNAs Acts in the Mammalian Brain. *Cell* **174**, 350-362.e17 (2018).
6. M. Piwecka, *et al.*, Loss of a mammalian circular RNA locus causes miRNA deregulation and affects brain function. *Science* **357**, eaam8526 (2017).
7. A. J. Zimmerman, *et al.*, A psychiatric disease-related circular RNA controls synaptic gene expression and cognition. *Mol Psychiatry* **25**, 2712–2727 (2020).
8. Y. J. Sun, J. Sebastian Espinosa, M. S. Hoseini, M. P. Stryker, Experience-dependent structural plasticity at pre- and postsynaptic sites of layer 2/3 cells in developing visual cortex. *Proceedings of the National Academy of Sciences* **116**, 21812–21820 (2019).
9. B. M. Hooks, C. Chen, Circuitry Underlying Experience-Dependent Plasticity in the Mouse Visual System. *Neuron* **106**, 21–36 (2020).
10. M. Majdan, C. J. Shatz, Effects of visual experience on activity-dependent gene regulation in cortex. *Nature Neuroscience* **9**, 650–659 (2006).
11. T. K. Hensch, E. M. Quinlan, Critical periods in amblyopia. *Vis Neurosci* **35**, E014 (2018).
12. M. Y. Frenkel, M. F. Bear, How monocular deprivation shifts ocular dominance in visual cortex of young mice. *Neuron* **44**, 917–923 (2004).
13. C. N. Levelt, M. Hübener, Critical-period plasticity in the visual cortex. *Annu Rev Neurosci* **35**, 309–330 (2012).
14. J. A. Gordon, M. P. Stryker, Experience-Dependent Plasticity of Binocular Responses in the Primary Visual Cortex of the Mouse. *Journal of Neuroscience* **16**, 3274–3286 (1996).

15. D. Tropea, A. Van Wart, M. Sur, Molecular mechanisms of experience-dependent plasticity in visual cortex. *Philosophical transactions of the Royal Society of London. Series B, Biological sciences* **364**, 341–55 (2009).
16. J. S. Espinosa, M. P. Stryker, Development and plasticity of the primary visual cortex. *Neuron* **75**, 230–249 (2012).
17. K. R. Jenks, K. Tsimring, J. P. K. Ip, J. C. Zepeda, M. Sur, Heterosynaptic Plasticity and the Experience-Dependent Refinement of Developing Neuronal Circuits. *Front Neural Circuits* **15**, 803401 (2021).
18. M. Sur, I. Nagakura, N. Chen, H. Sugihara, Mechanisms of plasticity in the developing and adult visual cortex. *Progress in Brain Research* **207**, 243–254 (2013).
19. D. Tropea, *et al.*, Gene expression changes and molecular pathways mediating activity-dependent plasticity in visual cortex. *Nature Neuroscience* **9**, 660–668 (2006).
20. T. Jakobi, A. Uvarovskii, C. Dieterich, circTools—a one-stop software solution for circular RNA research. *Bioinformatics* **35**, 2326–2328 (2019).
21. F. Chen, *et al.*, Nanoscale imaging of RNA with expansion microscopy. *Nature Methods* **13**, 679–684 (2016).
22. I. Nagakura, A. Van Wart, J. Petravicz, D. Tropea, M. Sur, STAT1 regulates the homeostatic component of visual cortical plasticity via an AMPA receptor-mediated mechanism. *J Neurosci* **34**, 10256–10263 (2014).
23. J. P. K. Ip, *et al.*, Major Vault Protein, a Candidate Gene in 16p11.2 Microdeletion Syndrome, Is Required for the Homeostatic Regulation of Visual Cortical Plasticity. *J Neurosci* **38**, 3890–3900 (2018).
24. C. L. Peebles, *et al.*, Arc regulates spine morphology and maintains network stability in vivo. *Proc Natl Acad Sci U S A* **107**, 18173–18178 (2010).
25. K. P. Berry, E. Nedivi, Spine Dynamics: Are They All the Same? *Neuron* **96**, 43–55 (2017).
26. A. C. McClelland, M. Hruska, A. J. Coenen, M. Henkemeyer, M. B. Dalva, Trans-synaptic EphB2–ephrin–B3 interaction regulates excitatory synapse density by inhibition of postsynaptic MAPK signaling. *Proceedings of the National Academy of Sciences* **107**, 8830–8835 (2010).
27. C. L. McCurry, *et al.*, Loss of Arc renders the visual cortex impervious to the effects of sensory experience or deprivation. *Nature neuroscience* **13**, 450–7 (2010).

28. J. D. Shepherd, *et al.*, Arc/Arg3.1 Mediates Homeostatic Synaptic Scaling of AMPA Receptors. *Neuron* **52**, 475–484 (2006).
29. X. You, *et al.*, Neural circular RNAs are derived from synaptic genes and regulated by development and plasticity. *Nat Neurosci* **18**, 603–610 (2015).
30. S. Chowdhury, *et al.*, Arc/Arg3.1 Interacts with the Endocytic Machinery to Regulate AMPA Receptor Trafficking. *Neuron* **52**, 445–459 (2006).
31. A. Rybak-Wolf, *et al.*, Circular RNAs in the Mammalian Brain Are Highly Abundant, Conserved, and Dynamically Expressed. *Molecular Cell* **58**, 870–885 (2014).
32. N. E. Clifton, S. Trent, K. L. Thomas, J. Hall, Regulation and Function of Activity-Dependent Homer in Synaptic Plasticity. *Mol Neuropsychiatry* **5**, 147–161 (2019).
33. G. H. Diering, *et al.*, Homer1a drives homeostatic scaling-down of excitatory synapses during sleep. *Science* **355**, 511–515 (2017).
34. V. Chokshi, B. Druciak, P. F. Worley, H. K. Lee, Homer1a is required for establishment of contralateral bias and maintenance of ocular dominance in mouse visual cortex. *Journal of Neuroscience* **39**, 3897–3905 (2019).
35. J. H. Hu, *et al.*, Homeostatic Scaling Requires Group I mGluR Activation Mediated by Homer1a. *Neuron* **68**, 1128–1142 (2010).
36. S. C. Martin, S. K. Monroe, G. H. Diering, Homer1a and mGluR1/5 Signaling in Homeostatic Sleep Drive and Output. *Yale J Biol Med* **92**, 93–101 (2019).
37. K. M. Tyssowski, *et al.*, Firing Rate Homeostasis Can Occur in the Absence of Neuronal Activity-Regulated Transcription. *J Neurosci* **39**, 9885–9899 (2019).
38. A. Rozov, A. R. Zivkovic, M. K. Schwarz, Homer1 gene products orchestrate Ca²⁺-permeable AMPA receptor distribution and LTP expression. *Front Synaptic Neurosci* **4**, 4 (2012).
39. D. Shin, M. Nam, Y. Yoon, M. Kim, Membrane-based hybridization capture of intracellular peptide nucleic acid. *Analytical Biochemistry* **399**, 135–137 (2010).
40. B. J. Yoon, G. B. Smith, A. J. Heynen, R. L. Neve, M. F. Bear, Essential role for a long-term depression mechanism in ocular dominance plasticity. *Proc Natl Acad Sci U S A* **106**, 9860–9865 (2009).
41. F. Ango, *et al.*, Dendritic and axonal targeting of type 5 metabotropic glutamate receptor is regulated by homer1 proteins and neuronal excitation. *J Neurosci* **20**, 8710–8716 (2000).

42. A. K. Hafez, *et al.*, A bidirectional competitive interaction between circHomer1 and Homer1b within the orbitofrontal cortex regulates reversal learning. *Cell Reports* **38**, 110282 (2022).
43. V. Chokshi, *et al.*, Input-Specific Metaplasticity in the Visual Cortex Requires Homer1a-Mediated mGluR5 Signaling. *Neuron* **104**, 736-748.e6 (2019).
44. N. Mellios, *et al.*, Regulation of neuronal circHomer1 biogenesis by PKA/CREB/ERK-mediated pathways and effects of glutamate and dopamine receptor blockade. *Res Sq* rs.3.rs-3547375 (2024). <https://doi.org/10.21203/rs.3.rs-3547375/v1>.
45. Y. Enuka, *et al.*, Circular RNAs are long-lived and display only minimal early alterations in response to a growth factor. *Nucleic Acids Research* **44**, 1370–1383 (2016).
46. Y. Zhang, *et al.*, The Biogenesis of Nascent Circular RNAs. *Cell Reports* **15**, 611–624 (2016).
47. C. Xu, *et al.*, Structure and plasticity of silent synapses in developing hippocampal neurons visualized by super-resolution imaging. *Cell Discovery* **6**, 1–11 (2020).
48. W. R. Jeck, *et al.*, Circular RNAs are abundant, conserved, and associated with ALU repeats. *RNA* **19**, 141–157 (2013).
49. D. Liang, J. E. Wilusz, Short intronic repeat sequences facilitate circular RNA production. *Genes and Development* **28**, 2233–2247 (2014).
50. Q. Zheng, *et al.*, Circular RNA profiling reveals an abundant circHIPK3 that regulates cell growth by sponging multiple miRNAs. *Nature Communications* **7**, 1–13 (2016).
51. N. R. Choudhury, *et al.*, Tissue-specific control of brain-enriched miR-7 biogenesis. *Genes and Development* **27**, 24–38 (2013).
52. T. B. Hansen, *et al.*, Natural RNA circles function as efficient microRNA sponges. *Nature* **495**, 384–388 (2013).
53. S. Memczak, *et al.*, Circular RNAs are a large class of animal RNAs with regulatory potency. *Nature* **495**, 333–338 (2013).
54. M. Rajman, G. Schratt, MicroRNAs in neural development: from master regulators to fine-tuners. *Development* **144**, 2310–2322 (2017).
55. D. B. Dudekula, *et al.*, CirclInteractome: A web tool for exploring circular RNAs and their interacting proteins and microRNAs. *RNA Biol* **13**, 34–42 (2016).

56. J. B. Dictenberg, S. A. Swanger, L. N. Antar, R. H. Singer, G. J. Bassell, A Direct Role for FMRP in Activity-Dependent Dendritic mRNA Transport Links Filopodial-Spine Morphogenesis to Fragile X Syndrome. *Dev Cell* **14**, 926–939 (2008).
57. R. Fujii, *et al.*, The RNA binding protein TLS is translocated to dendritic spines by mGluR5 activation and regulates spine morphology. *Curr Biol* **15**, 587–593 (2005).
58. Y. Kanai, N. Dohmae, N. Hirokawa, Kinesin Transports RNA: Isolation and Characterization of an RNA-Transporting Granule. *Neuron* **43**, 513–525 (2004).
59. D. Kim, J. M. Paggi, C. Park, C. Bennett, S. L. Salzberg, Graph-based genome alignment and genotyping with HISAT2 and HISAT-genotype. *Nat Biotechnol* **37**, 907–915 (2019).
60. Y. Liao, G. K. Smyth, W. Shi, featureCounts: an efficient general purpose program for assigning sequence reads to genomic features. *Bioinformatics* **30**, 923–930 (2014).
61. M. I. Love, W. Huber, S. Anders, Moderated estimation of fold change and dispersion for RNA-seq data with DESeq2. *Genome Biology* **15**, 550 (2014).
62. C. Trapnell, *et al.*, Differential gene and transcript expression analysis of RNA-seq experiments with TopHat and Cufflinks. *Nature Protocols* **7**, 562–578 (2012).
63. M. E. Ritchie, *et al.*, limma powers differential expression analyses for RNA-sequencing and microarray studies. *Nucleic Acids Research* **43**, e47 (2015).
64. G. Yu, L. G. Wang, Y. Han, Q. Y. He, clusterProfiler: an R package for comparing biological themes among gene clusters. *OMICS* **16**, 284–287 (2012).
65. S. M. Asano, *et al.*, Expansion Microscopy: Protocols for Imaging Proteins and RNA in Cells and Tissues. *Current Protocols in Cell Biology* **80**, e56 (2018).
66. T. Ku, *et al.*, Multiplexed and scalable super-resolution imaging of three-dimensional protein localization in size-adjustable tissues. *Nat Biotechnol* **34**, 973–981 (2016).
67. J. Park, *et al.*, Epitope-preserving magnified analysis of proteome (eMAP). *Sci Adv* **7**, eabf6589 (2021).
68. Y. Wang, *et al.*, Astrocyte-secreted IL-33 mediates homeostatic synaptic plasticity in the adult hippocampus. *Proc Natl Acad Sci U S A* **118**, e2020810118 (2021).
69. T. Chen, H. L. He, G. M. Church, Modeling gene expression with differential equations. *Pac Symp Biocomput* 29–40 (1999).

70. A. Bachmayr-Heyda, *et al.*, Correlation of circular RNA abundance with proliferation--exemplified with colorectal and ovarian cancer, idiopathic lung fibrosis, and normal human tissues. *Sci Rep* **5**, 8057 (2015).

Figure Legends

Figure 1. Experience-dependent circRNAs in V1 identified through MD.

(A) Timeline and schematic of 3-day MD RNAseq screen. (B) Volcano plot (upper) and heatmap (lower) of mRNA sequencing of V1 after 3-day MD (n = 3 mice per group). (C) Volcano plot (upper) and heatmap (lower) of circRNA sequencing of V1 after 3-day MD (n = 3 mice per group). The ipsilateral hemisphere (ipsi) served as a control for MD induced changes in the contralateral hemisphere (contra) for both mRNA and circRNA expression. (D) GO enrichment of mRNA differentially-expressed after 3-day MD. DEG, differentially-expressed gene. (E) Fold change of differentially-expressed circRNAs and their mRNA isoforms after 3-day MD. The mouse and brain silhouette were adapted from <https://doi.org/10.5281/zenodo.8044766> and <https://doi.org/10.5281/zenodo.3925971>.

Figure 2. *circHomer1* expression is regulated by experience-dependent plasticity and upregulated during the ocular dominance critical period.

(A) The mouse *Homer1* gene encodes long and short versions of the synaptic protein Homer1 and a noncoding circRNA, *circHomer1*. (B) Visualization of *circHomer1* by ExFISH in V1 neurons expressing tdTomato. Scale bar = 10 μm (estimated to be 2.85 μm prior to 3.5x expansion). (C) RT-qPCR quantification of selected mRNAs and *circHomer1* after 3-day or 7-day MD (n = 3-4 mice per group, paired t-test). (D) *circHomer1* (left), *Homer1a* (middle), and *circTulp4* (right) expression measured by RT-qPCR at several timepoints in mouse V1 across development and into adulthood (n = 3-6 mice per group, one-way ANOVA following Tukey multiple comparisons). Data are presented as mean \pm SEM. *p < 0.05, **p < 0.01, ***p < 0.001.

Figure 3. *circHomer1* depletion delays the expression of ocular dominance plasticity in V1 following MD.

(A) Mice were injected with either sh-*circHomer1* or sh-scramble virus at P15, a craniotomy was performed at P22 to implant a cranial window, then a pre-MD optical imaging session was done and the contralateral eye-lid sutured at P25. After either 3-

day or 7-day MD, the eyelid was reopened and post-MD imaging done. (B) Example retinotopic maps from a sh-circHomer1 mouse, obtained with optical imaging. The color corresponds with different phases of the visual stimulus (consistent with the visual field map) and brightness shows the amplitude of cortical response. Top, contralateral closed-eye responses, pre-MD (left) and after 7-day MD (right). Bottom, ipsilateral open-eye responses. Scale bar = 500 μ m. (C) ODI changes after 3-day or 7-day MD for mice injected with sh-scramble or sh-circHomer1 virus. Each dot shows the average ODI for one animal, and grey lines show the change of ODI for one animal (n= 5-11 mice per group, mixed-effects model following Holm-Sidak multiple comparisons test). (D) Normalized response amplitudes driven by the contralateral (left) and ipsilateral (right) eyes (n= 5-11 mice per group, mixed-effects model following Holm-Sidak multiple comparisons test). Data are presented as mean \pm SEM. *: compared to preMD: sh-scramble; †: compared to preMD: sh-circHomer1. *, †p < 0.05; **, ††p < 0.01; †††p < 0.001.

Figure 4. Depletion of *circHomer1* affects spine morphology of V1 neurons.

(A) A schematic of tissue preparation and eMAP. (B) Neurons expressing both GFP and RFP (denoting shRNA) were selected for analysis (left). Dendritic spines were classified into four categories based on their morphology (right). Scale bars = 100 μ m (left, estimated to be 33.33 μ m prior to 3x expansion), and 10 μ m (right, estimated to be 3.33 μ m prior to 3x expansion). (C) Representative images showing apical dendrites of layer 2/3 neurons in V1 in the No MD, 3-day MD, and 7-day MD condition from the sh-scramble (top) or sh-circHomer1 (bottom) group. Arrows indicate different types of dendritic spines. Scale bar = 10 μ m (estimated to be 3.33 μ m prior to 3x expansion). (D) Density of mushroom spines, and immature spines (stubby spines, thin spines and filopodia) on apical dendrites of layer 2/3 neurons in V1 in the No MD, 3-day MD, and 7-day MD condition from the sh-scramble (grey) or sh-circHomer1 (pink) group (n=8-10 dendrites from 3 mice per group, values were normalized to 3x expansion factor, two-way ANOVA following Tukey multiple comparisons). (E) Spine morphology types as a percentage of total spines. The percentage of mushroom spines are labeled on the bar. (F) Volume of dendritic spines on apical dendrites (same data as in D and E, values were normalized to 3³ expansion factor, two-way ANOVA following Tukey multiple

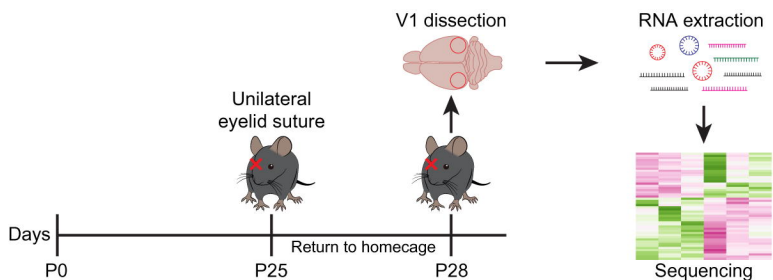
comparisons). (G) Distribution of spine volume in sh-scramble and sh-circHomer1 mice in the 3 conditions (n=235-334 dendritic spines from 3 mice per group). Data are presented as mean \pm SEM. *: compared to No MD: sh-scramble. *p < 0.05; **p < 0.01; ***p < 0.001.

Figure 5. Trafficking of surface AMPA receptors following MD is regulated by *circHomer1*.

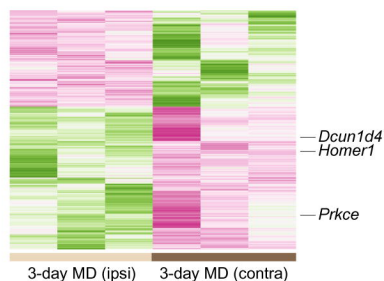
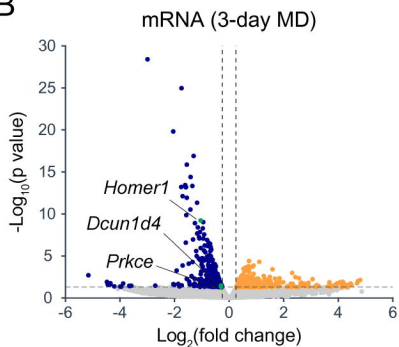
(A) Schematic graph showing a model that *circHomer1* potentially upregulates AMPA receptor endocytosis via upregulating synaptic Arc. (B) Left: Western blot of cell surface expression of GluA1 in V1 of mice after MD. Scr, sh-scramble; KD, sh-circHomer1. Right: Quantification of surface GluA1 level (n=4 mice per group, two-way ANOVA following Tukey multiple comparisons). (C) Representative images showing 3D reconstruction of a segment of dendrites staining with GFP and Arc after eMAP processing. Scale bar = 5 μ m (estimated to be 1.67 μ m prior to 3x expansion). (D) Representative images of 3D-reconstructed Arc puncta at dendritic spines of V1 neurons after MD. Scale bar = 1 μ m (estimated to be 0.33 μ m prior to 3x expansion). (E) Percentage of dendritic spines containing Arc puncta (n=8-11 dendrites from 3 mice per group, two-way ANOVA following Tukey multiple comparisons). (F) Arc puncta volume at dendritic spines (n=29-71 puncta from 8-11 dendrites from 3 mice per group, values were normalized to 3³ expansion factor, two-way ANOVA following Tukey multiple comparisons). (G) The ratio of Arc puncta volume and corresponding dendritic spine volume (n=20-51 dendritic spines from 8-11 dendritic spines from 3 mice per group, two-way ANOVA following Tukey multiple comparisons). *: compared to No MD: sh-scramble; †: compared to No MD: sh-circHomer1. Data are presented as mean \pm SEM. *, †p < 0.05; **, ††p < 0.01; ***, †††p < 0.001.

Figure 1

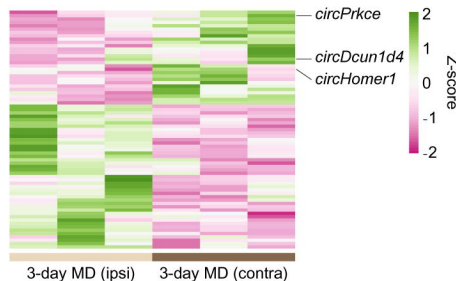
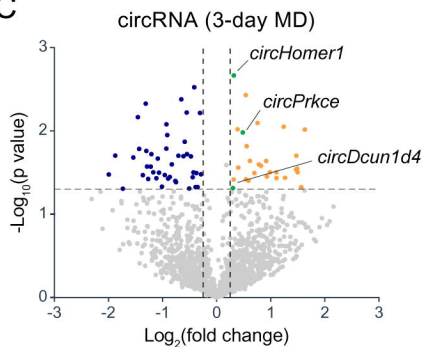
A



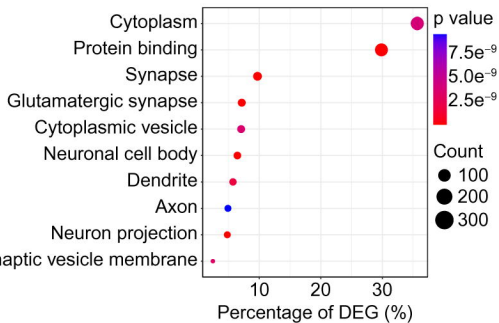
B



C



D



E

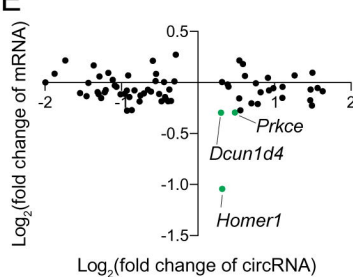
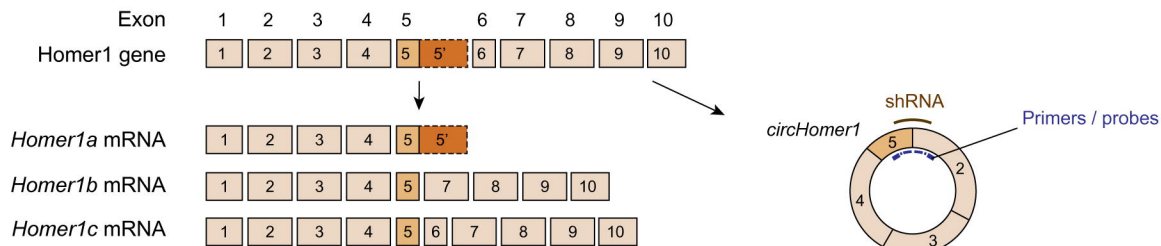
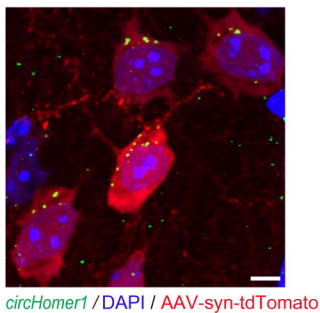


Figure 2

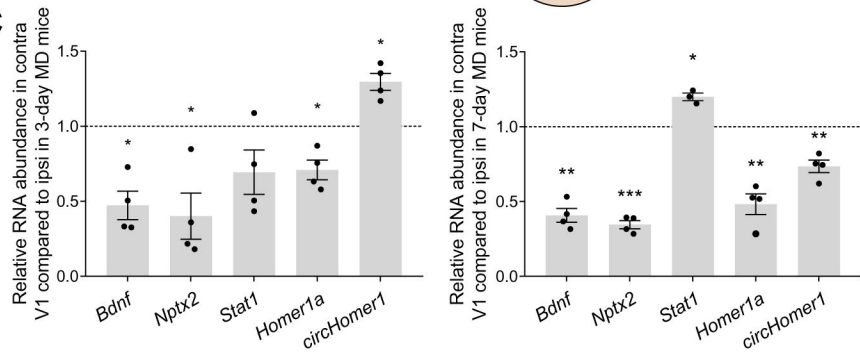
A



B



C



D

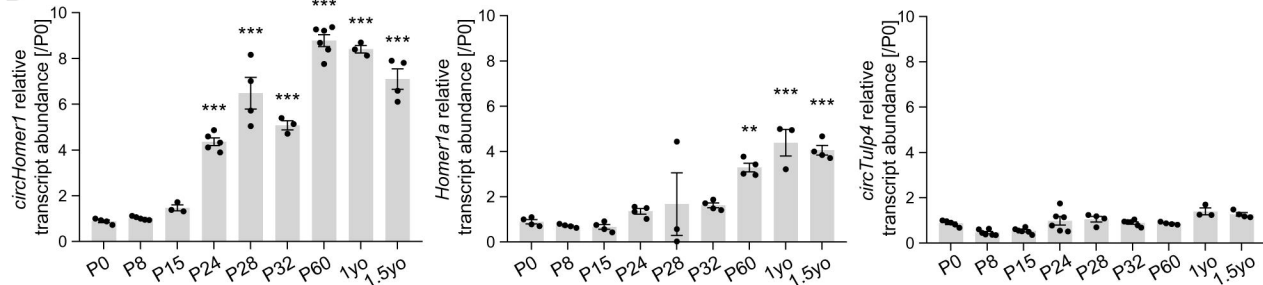


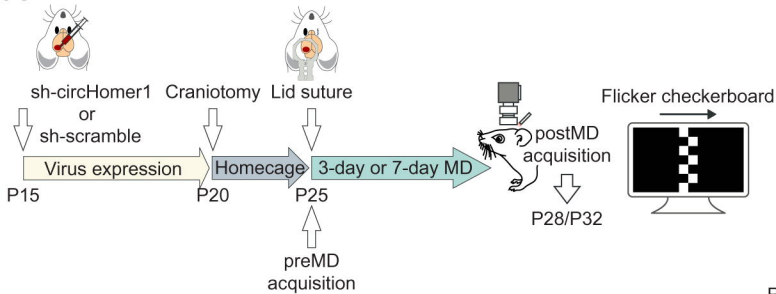
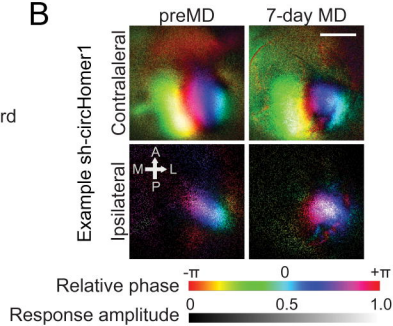
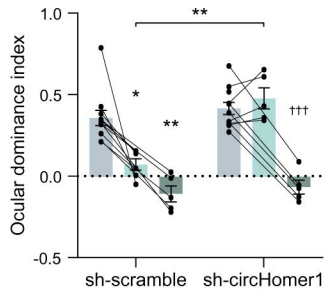
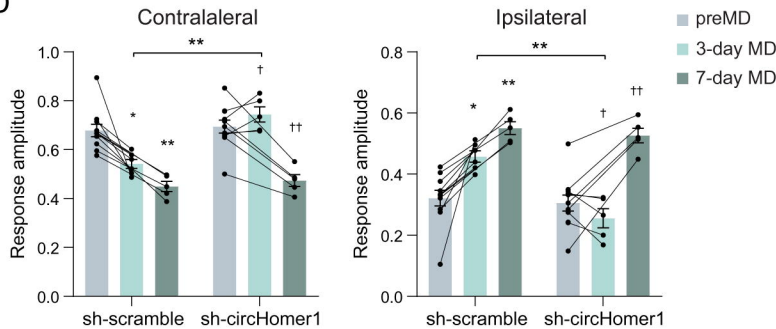
Figure 3**A****B****C****D**

Figure 4